Applied Catalysis B: Environmental 179 (2015) 54–60

Contents lists available at ScienceDirect

Applied Catalysis B: Environmental

journal homepage: www.elsevier.com/locate/apcatb

Realizing nanosized interfacial contact *via* constructing $BiVO_4/Bi_4V_2O_{11}$ element-copied heterojunction nanofibres for superior photocatalytic properties

Chade Lv, Gang Chen*, Jingxue Sun*, Yansong Zhou, Shuo Fan, Congmin Zhang

Department of Chemistry, Harbin Institute of Technology, Harbin 150001, PR China

ARTICLE INFO

Article history:
Received 16 February 2015
Received in revised form 5 May 2015
Accepted 11 May 2015
Available online 14 May 2015

Keywords:
Nanosized interfacial contact
$BiVO_4/Bi_4V_2O_{11}$
Element-copied heterojunction
Photocatalytic properties

ABSTRACT

Heterojunction with nanosized interfacial contact stands out in promoting the transfer photoinduced interfacial carriers. Herein, a heterojunction with nanosized interfacial contact was designed by constructing $BiVO_4/Bi_4V_2O_{11}$ element-copied heterojunction nanofibres. The heterojunction was formed by combining $BiVO_4$ nanofibres and embedded $Bi_4V_2O_{11}$ nanocrystals. They offered favourable interfacial contact on nanosized level. The photocatalytic performance of heterojunction nanofibres with nanosized interfacial contact were indicated to be markedly enhanced compared with that of pure $BiVO_4$ nanofibres. Furthermore, we also observed a 10-fold enhancement in the photocurrent intensity for the heterojunction nanofibres with nanosized interfacial contact, indicating the enhancement of photocatalytic properties was attributed to the nanosized interfacial contact with wonderful interfacial photoinduced carriers transfer behavior.

1. Introduction

Nowadays, environmental contamination has become the most urgent issue to solve. With the purpose of meeting the requirements of future environmental technologies, constructing heterojunction photocatalysts by combining them with metal/semiconductors has drawn a lot of attentions owing to its outstanding effectiveness in promoting the separation of photoinduced carriers at the interfaces of two semiconductors [1–5].

Constructing heterojunction with nanosized interfacial contact could further promote the separation and transfer of photoinduced carriers due to their favourable interfacial contact and shorten transfer pathway [6]. Moreover, nanosized interfacial contact makes it possible to produce unique interface states for rapid interfacial photoinduced carriers transfer [7]. Very recently, many kinds of novel heterojunctions with nanosized interfacial contact have been designed and adequately demonstrated to show enhanced catalytic or electrocatalytic properties, due to the synergetic effects of two semiconductors in charge transfer, nanosized interfacial collaboration, or structural strain at nanoszied interfaces [8–10]. For instance, Wang's group reported that nanosized interfaces between the CdS nanowires and $ZnIn_2S_4$ nanosheets could induce the delocalized interface states, thus facilitating the charge carriers transfer and enhancing the performance in the photoelectrochemistry [11]. The matches in lattice and dangling bonds between the two semiconductors are responsible for the formation of nanosized interfaces. In a certain sense, the reasonable design and careful construction of heterojunction with nanosized interfacial contact could contribute to fabricate excellent photocatalysts. Nevertheless, owing to the structural stress and mismatch in lattice of as-selected semiconductors, constructing heterojunction optionally could prevent us from obtaining nanosized interfacial contact [12]. Therefore, it is necessary to employ appropriate semiconductor candidates for constructing heterojunction with nanoszied interfacial contact.

Many nontypical stoichiometric semiconductor photocatalysts, such as Bi_3O_4Cl [13], $Bi_{24}O_{31}Cl_{10}$ [14], $Bi_{24}O_{31}Br_{10}$ [15,16], Bi_5O_7I [17], $Bi_4V_2O_{11}$ [18], $Bi_2VO_{5.5}$ [19] and $W_{18}O_{49}$ [20,21], could be qualified as ideal candidates for the construction of heterojunction with nansozied interfacial contact. These nontypical stoichiometric photocatalysts exhibit excellent photocatalytic activity owing to their unique band structure, more strong mobility of charge carriers and effective capacity in separation of photoinduced electron-hole pairs, compared with their corresponding typical stoichiometric semiconductor photocatalysts (BiOX (X = Cl, Br, I), $BiVO_4$ and WO_3). More significantly, they also possess consistent element composition and approximate crystalline architecture relative to their corresponding typical stoichiometric semiconductor

* Corresponding authors. Tel.: +86 451 86413753; fax: +86 451 86413753.
E-mail addresses: gchen@hit.edu.cn (G. Chen), jxsun@hit.edu.cn (J. Sun).

http://dx.doi.org/10.1016/j.apcatb.2015.05.022
0926-3373/

photocatalysts. Therefore, it is envisaged that it could possibly lead to the formation of heterojunction with nanosized interfacial contact *via* combining them with their corresponding typical stoichiometric semiconductors. To turn out the feasibility of this envisagement, we combine $BiVO_4$ with $Bi_4V_2O_{11}$ to construct a element-copied heterojunction. And to the best of our knowledge, this is the first time a fabrication and photocatalytic properties of $BiVO_4/Bi_4V_2O_{11}$ element-copied heterojunction is reported.

However, nanosized interfacial contact could easily aggregate to minimize the surface energy [22]. In order to avoid the aggregation of nanosized interfacial contact, we take advantage of one-dimensional nanomaterials to construct heterojunction because 1D nanomaterials could serve as outstanding substrates [23–25]. Therefore, it is of importance to fabricate one-dimensional $BiVO_4/Bi_4V_2O_{11}$ heterojunction to realize the formation of high density of nanosized interfacial contact.

In this paper, $BiVO_4/Bi_4V_2O_{11}$ heterojunction nanofibres were fabricated *via* a facile electrospinning process. The $Bi_4V_2O_{11}$ nanocrystals with well-dispersed distribution were embedded in the $BiVO_4$ nanofibres to form nanosized interfacial contact. The heterojunction nanofibres with nanosized interfacial contact exhibited much higher photocatalytic activity than pure $BiVO_4$ nanofibres. The nanosized interfacial contact realized a more effective separation and transfer of photoinduced carriers to obtain a much better properties in the photocatalysis. Furthermore, the formation and photocatalytic mechanism of $BiVO_4/Bi_4V_2O_{11}$ element-copied heterojunction is investigated.

2. Experimental

2.1. Preparation and characterisations

All reagents were of analytical purity, received from Aladdin reagents company, and used without further purification. In a typical synthesis, 0.840 g (4.0 mmol) of citric acid was dissolved in 26 mL of DMF (*N*,*N*-dimethylformamide) with magnetic stirring at room temperature, and then 0.647 g (1.33 mmol) of $Bi(NO_3)_3{\cdot}5H_2O$ was added into the mixture. After the $Bi(NO_3)_3{\cdot}5H_2O$ dissolved, 0.152 g (1.30 mmol) NH_4VO_3 was added slowly into the $Bi(NO_3)_3$ solution. Afterward, 2.0 g PVP ($Mw \approx 1{,}300{,}000$) was added slowly into above solution. Thus the spinnable precursor sols were obtained after continuous stirring 12 h. All the precursor sols were transferred into a syringe which was attached to a stainless steel needle with inner diameter of 0.901 mm. The positive voltage applied to the tip was 18 kV and the distance between the needle tip and the collector was 12 cm. And the feeding rate was controlled as 1.0 mL h^{-1}. The as-spun fibres were collected from a collector plate (Al foil).

Then, the as-spun fibres were put into an air-atmosphere programmable chamber furnace for heat treatment. The as-spun fibres were annealed at 500 °C for 2 h with a ramp rate of 1 °C min^{-1}. The as-calcinated product was denoted as BVO-1. Pure $BiVO_4$ nanofibres were fabricated by employing same mole amounts of $Bi(NO_3)_3{\cdot}H_2O$ and NH_4VO_3 (BVO-0), while the mole ration is 2:1 for pure $Bi_4V_2O_{11}$ nanofibres (denoted as BVO-4). In addition, the ratios were set as 1.7:1.3 and 2.1:1.3 to obtain comparative heterojunction nanofibres without favourable nanosized interfacial contact, and the final as-calcinated samples were denoted as BVO-2 and BVO-3, respectively. The amount of V is fixed.

The structure of the obtained samples were confirmed by X-ray diffraction (XRD) on Rigaku D/max-2000 diffractometer with Cu Kα radiation ($\lambda = 0.15406$ nm). Diffraction patterns were collected from 10° to 90° at a speed of 4° min^{-1} with a scan width of 0.02°. The morphology of the samples were observed by a Camscan MX2600FE field emission scanning electron micro-scope (FE-SEM). The operating voltage was set to 20 kV and the samples were prepared by dropping the pre-ultrasonic-dispersed (10 min) ethanol turbid liquid onto the chip of silicon. Transmission electron microscopy (TEM) and high-resolution TEM (HRTEM) of the hierarchical structures were carried out on FEI Tecnai G2 S-Twin operating at 300 kV. UV–vis diffuse reflectance spectra were acquired by a spectrophotometer (TU-190) and $BaSO_4$ was used as the reflectance standard. X-ray photoelectron spectroscopy (XPS) was accomplished using a PHI-5702 multifunctional X-ray photoelectron spectrometer with a pass energy of 29.35 eV and an Mg Kaline excitation source. Raman spectra were recorded on a HORIBA Xplore instrument with an Ar^+ laser source of 532 nm wavelength in a macroscopic configuration.

2.2. Photocatalytic and photoelectrochemical measurements.

The photocatalytic activities of the samples were evaluated by the degradation of RhB under visible light by using a 300 W Xe lamp (Trusttech PLS-SXE 300, Beijing) with a cutoff filter ($\lambda \geq 400$ nm). The initial concentration of RhB was 10 mg/L. 0.05 g photocatalysts were put into 100 mL of RhB solution. Before the photodegradation experiments were initiated, the suspension was magnetically stirred in the dark for 55 min to reach adsorption–desorption equilibrium and sonicated for 5 min. Once the photodegradation experiment started, at given time intervals, 4 mL aliquots solution were sampled and centrifuged to remove the photocatalysts. The filtrates were analysed by the variations of the absorption-band maximum (554 nm).

The photocurrent transient response measurement was carried out at the open circuit potential. The light source employed was a 300 W Xe light source. CHI604C electrochemical working station with a standard three-compartment cell was employed to measure the photoelectrochemical characteristics of the samples. FTO glass with photocatalysts coated was used as working electrode and a piece of Pt sheet, a Ag/AgCl electrode and 0.5 M sodium sulfate served as the counter electrode, reference electrode and electrolyte, respectively.

3. Results and discussion

The XRD pattern, SEM and TEM images of BVO-1 are shown in Fig. 1. The XRD pattern of BVO-1 can be assigned to monoclinic scheelite $BiVO_4$ (JCPDS no. 14-0688) and monoclinic $Bi_4V_2O_{11}$ (JCPDS no. 82-1481), indicating that the target product could be obtained by this strategy (Fig. 1a). As Fig. 1b shows, the as-spun fibres are one-dimensional uniform texture structure with glossy surface. Furthermore, the diameter of as-spun nanofibres is about 400–600 nm and the length is about several micrometers. After calcination, the BVO-1 could retain the one-dimensional structure. However, the disappearance of organic composition leads to the shrinkage and porosity of the fibres. And the diameter decreases to 200–400 nm (Fig. 1c). TEM image (Fig. 1d) confirms that nanofibres are one-dimensional with diameters of about 200–400 nm, which agrees well with that revealed by the SEM images. As observed from the HRTEM image shown in Fig. 1e, nanocrystals with a size of 5–10 nm are embedded in the fibres with well-dispersed distribution. Fig. 1f demonstrates the substrate fibres are $BiVO_4$, which is confirmed by the interplanar spacing of 0.308 nm, corresponding well to the (1 2 1) plane of monoclinic $BiVO_4$. Meanwhile, the interplanar spacings of 0.332 nm verifies the (0 0 5) plane of the embedded $Bi_4V_2O_{11}$ nanocrystals. Obviously, the $BiVO_4/Bi_4V_2O_{11}$ heterojunctions are formed with favourable nanosizd interfacial contact (Fig. 1e and f, Fig. S1). The insert image in Fig. 1f shows the legible diffraction spots of the corresponding SAED patterns,

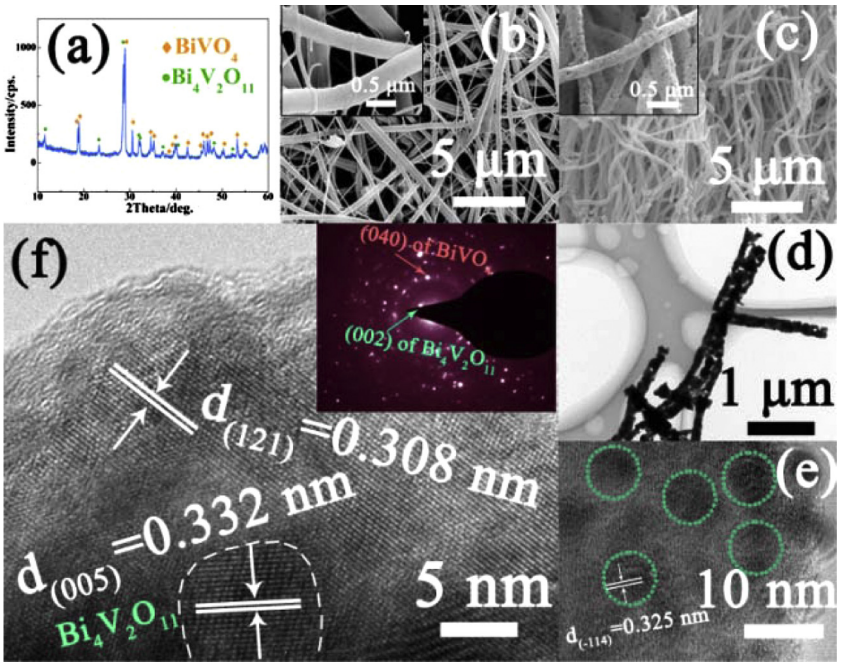

Fig. 1. (a) XRD pattern of BVO-1; (b), (c) SEM images of as-spun fibres and as-calcinated nanofibres, respectively; (d), (e) TEM images of the BVO-1 nanofibres; (f) HRTEM of BVO-1 and the insert image is SAED pattern in BVO-1 nanofibres.

demonstrating the existence of $BiVO_4$ and $Bi_4V_2O_{11}$ in the BVO-1 nanofibres.

The XRD patterns of the as-calcinated samples are shown in Fig. 2. BVO-0 is assigned to monoclinic $BiVO_4$ (JCPDS No. 14-0688) without any impurity, while only characteristic peaks of $Bi_4V_2O_{11}$ could be observed in BVO-4. For the heterojunction samples, the diffraction peaks of $Bi_4V_2O_{11}$ and $BiVO_4$ could be simultaneously observed in BVO-1, BVO-2 and BVO-3.

Fig. 3a–d displays the SEM images of as-calcinated nanofibres except BVO-1. The BVO-0 nanofibres exhibit one-dimensional morphology ranged from 500 nm to 800 nm. With the increase of Bi amounts, the SEM images shown in Fig. 4b–d indicate that the nanofibres' retiform morphology is scarcely changed while the diameter reduces gradually. Photocatalysts formation and organic ingredient decomposition take place simultaneously during the calcination of as-spun fibres. Thus, the heat treatment process could be imbalanced when changing the ratio of inorganic and organic ingredient [26,27]. As a result, the alteration of the ratio could determine the morphology of as-calcinated product after calcination.

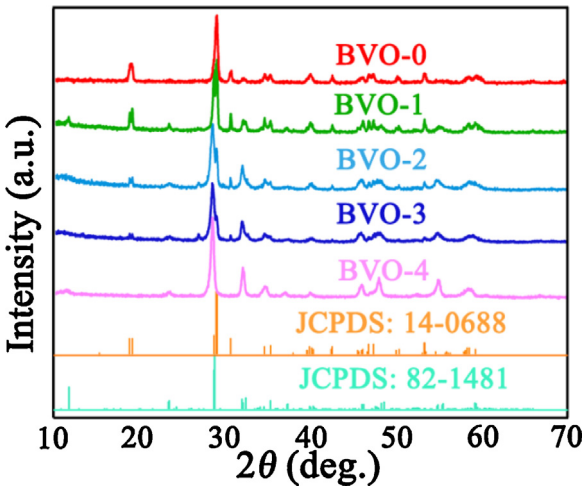

Fig. 2. XRD patterns of the as-calcinated samples

As shown above, as Bi increases, the morphology of the heterojunction fibres changes obviously. To figure out whether BVO-2 and BVO-3 heterojunction nanofibres are rich in nanosized interfacial contact, TEM characterization is performed. Fig. 4a and c confirm that BVO-2 and BVO-3 nanofibres are one-dimensional with diameters of about 100–300 nm. The presence of $BiVO_4$ and $Bi_4V_2O_{11}$ could be verified in HRTEM images of BVO-2 and BVO-3 (Fig. 4b and d). Nevertheless, the content of nanosized interfacial contact reduced dramatically because the $Bi_4V_2O_{11}$ is not well-dispersed in BVO-2 and BVO-3. Moreover, single crystalline nature of $Bi_4V_2O_{11}$ could also be observed in HRTEM image and SAED pattern of BVO-2 (Fig. S2), demonstrating the $BiVO_4/Bi_4V_2O_{11}$ heterojunctions are not equably distributed. The overmuch employment of Bi leads to the formation of $Bi_4V_2O_{11}$ particles with large sizes, which might contribute to this reduction of nanosized interfacial contact.

Based on above results, a reasonable formation mechanism for nanosized interfaces in BVO-1 is proposed (Fig. 5). The Bi ions, V ions, critic acid and PVP are distributed uniformly in the spinnable sols. After electrospinning, as-spun fibres are formed with well-dispersed distribution of each ingredient. At the calcination stage, the thermal decomposition of the Bi, V precursor and PVP comes into being, which relieves the interference and triggers the nucleation and growth of $BiVO_4$. As a rule, Bi ions and V ions are consumed with a typical stoichiometric ratio (1:1) to form $BiVO_4$ at the initial stage. However, the ratio between Bi and V tends to 2:1 as it continues, which will result in $Bi_4V_2O_{11}$ nucleating. When the ratio approach 2:1, the $BiVO_4$ nanoparticles have been formed with large size and unreacted inorganic ingredient has been decrease dramatically. Besides, PVP might not decompose completely. Therefore, the growth of $Bi_4V_2O_{11}$ is impeded and the size of $Bi_4V_2O_{11}$ particles is restricted innanoscale. As the proposed formation process, employment of $Bi_4V_2O_{11}$ to construct element-copied heterojunction with $BiVO_4$ can realize the formation of nanosized interfacial contact.

XPS and Raman measurements are perforemed to investigate the interfacial interactions caused by constructing heterojunction

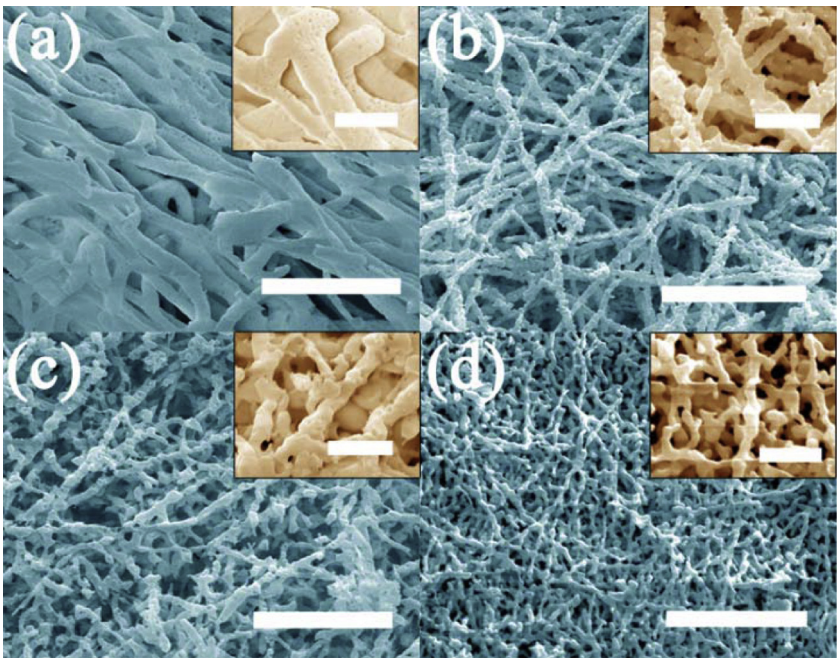

Fig. 3. SEM images of BVO-0 (a), BVO-2 (b), BVO-3 (c), and BVO-4 (d); the scale bars = 5 μm (1 μm for insert images)

with nanosized interfacial contact. XPS analysis of BVO-0, BVO-1 and BVO-4 is employed, and the corresponding results are shown in Fig. 6a–c. The Bi4f spectra of BVO-0, BVO-1 and BVO-4 nanofibres are displayed in Fig. 6a. Obviously, two symmetric peaks are displayed in the spectra, indicating the Bi ions are Bi^{3+} [28,29]. The Bi4f peaks in BVO-1 shift about 0.1 eV towards lower binding energies relative to BVO-0. The V2p of BVO-0, BVO-1 and BVO-4 are analysed in Fig. 6b. It illustrates that the V ions are V^{5+} in all the samples [30,31]. For BVO-1, the V2p peaks shift about 0.4 eV towards higher binding energies compared with that of BVO-0. Interestingly, a new peak appears at 520.2 eV in BVO-1, which is assigned to the O1s satellite peak [32]. The additional satellite peak results from the hybridization between V-3d and O-2p levels, indicating the formation of V—O bonds at the interface between the $BiVO_4$ nanofibres and embedded $Bi_4V_2O_{11}$ nanocrystals. Fig. 6c shows the O1s peaks of the samples. For pure $BiVO_4$ and $Bi_4V_2O_{11}$ nanofibres, the peak centered at 529.1 eV and 529.5 eV corresponded to the O 1s. However, the O 1s peak on the curves of the BVO-1 shift about 0.4 eV towards the higher binding enegies versus that of BVO-0 and a small peak appears at 533.5 eV which could be attributed to surface adsorbed oxygen [32].

As reported, the increase/decrease in electron concentration could enhance/reduce the electron screening effect, leading to weakening/strengthening the binding energy [33]. Thus, for this case, we believe that the higher binding energy shifts of V and O in BVO-1 are attributed to the decreased electron concentration of

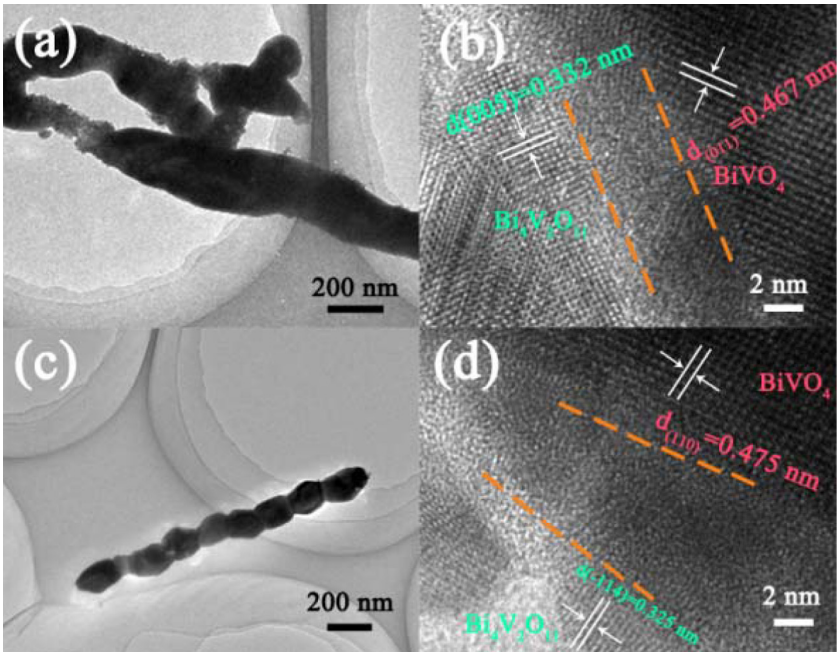

Fig. 4. TEM and HRTEM images of BVO-2 (a,b) and BVO-3 (c,d).

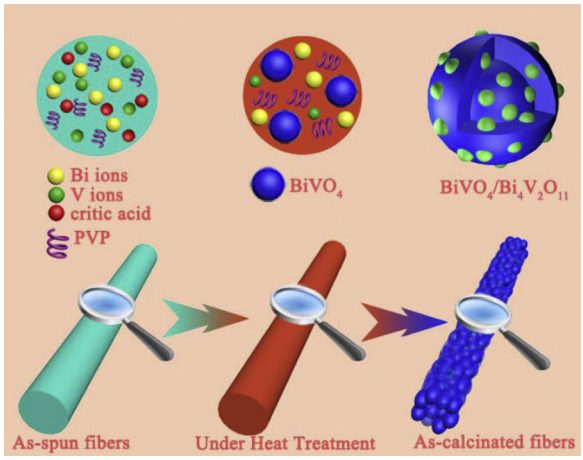

Fig. 5. Formation mechanism of nanosized interfacial contact in $BiVO_4/Bi_4V_2O_{11}$ heterojunction.

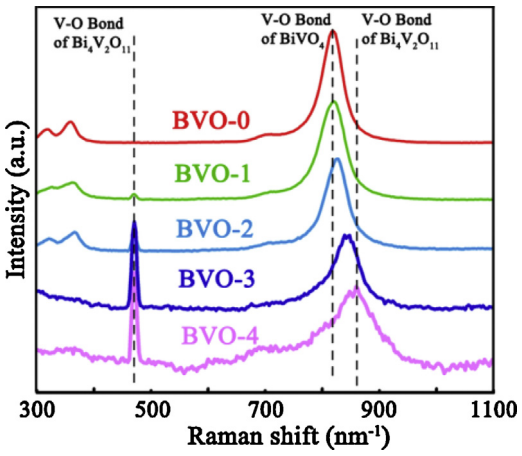

Fig. 7. Raman spectra of as-calcinated samples.

$BiVO_4$ nanofibres and increased electron concentration of $Bi_4V_2O_{11}$ nanocrystals caused by the electron transfer from the $BiVO_4$ nanofibres to $Bi_4V_2O_{11}$ nancrystals. However, for Bi 4f peaks, the shift towards lower binding energy could be attributed to the formation of Bi-V bond at the interface. The higher electronegativity of Bi could lead to the increase of electron concentration, which could enhance the electron screening effect. Thus, the Bi 4f peaks shift towards lower binding energy. Above results confirm that interfacial chemical bonding is formed to construct heterojunction between $BiVO_4$ nanofibres and embedded $Bi_4V_2O_{11}$ nanocrystals, which could be an expedite interface for promoting the interfacial photoinduced carriers transfer.

Fig. 7 shows the Raman spectra of as-calcinated samples. Raman bands around 470 cm^{-1} and 826 cm^{-1} assigned to V—O band of $Bi_4V_2O_{11}$ are gradually stronger as the content of $Bi_4V_2O_{11}$ increases [34,35]. Interestingly, taking BVO-0 as a reference, the Raman band shifting in BVO-1 could result from the formation of nanosized heterojunction, because the nanosized interfacial contact might cause intrinsic stresses on the crystal structure and change the periodicity of the lattice [36,37]. Hence, Raman spectra further affirm some interactions between the embedded $Bi_4V_2O_{11}$ nanocrystals and $BiVO_4$ nanofibres, which could offer wonderful pathways for rapid separation and transfer of photoinduced electron-hole pairs.

To probe the photocatalytic performance, the as-calcianted samples are evaluated by the photocatalysis degradation of RhB under visible light ($\lambda \geq 400$ nm). Fig. 8 shows the photocatalytic decomposition rate of different as-calcinated samples. Among the samples, BVO-1 exhibits a much higher photocatalytic performance than other samples. Moreover, the photocatalytic reduction of Cr(VI) experiment was carried out and the BVO-1 also exhibits the

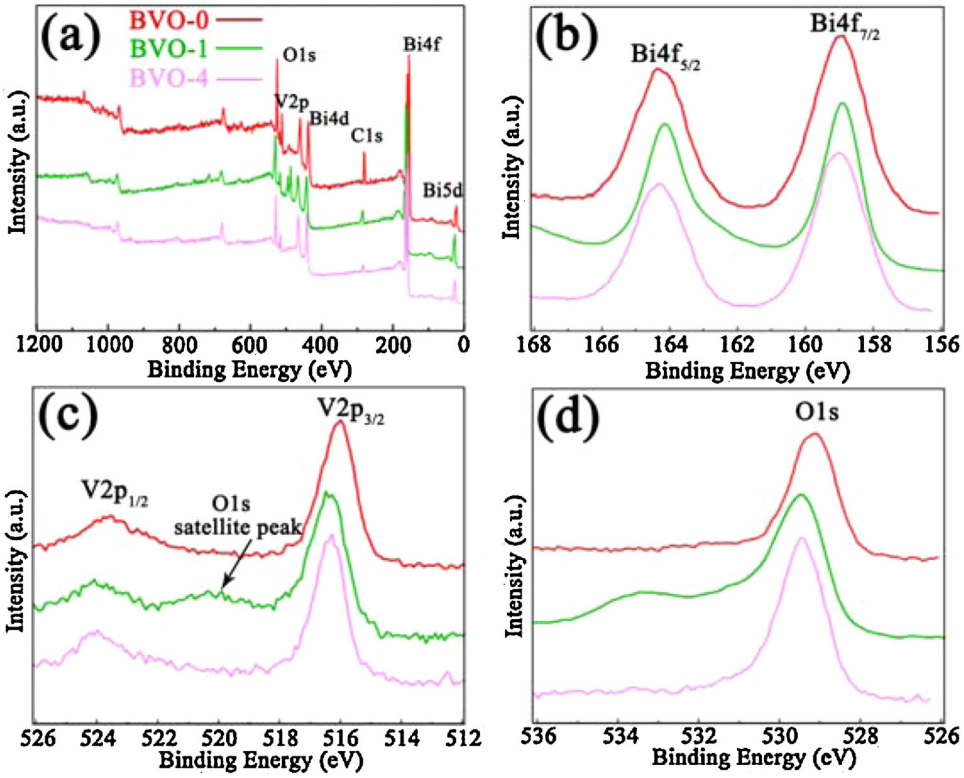

Fig. 6. XPS spectra of BVO-0, BVO-1 and BVO-4; full spectra (a) Bi 4f (b) V 2p (c) O 1s (d).

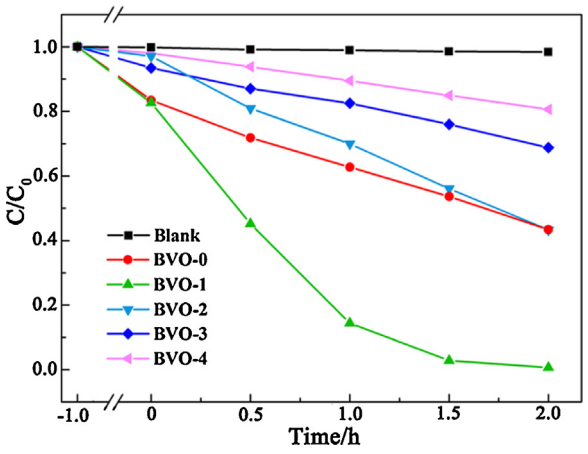

Fig. 8. Dynamic curves of RhB solution over as-calcinated samples under visible light.

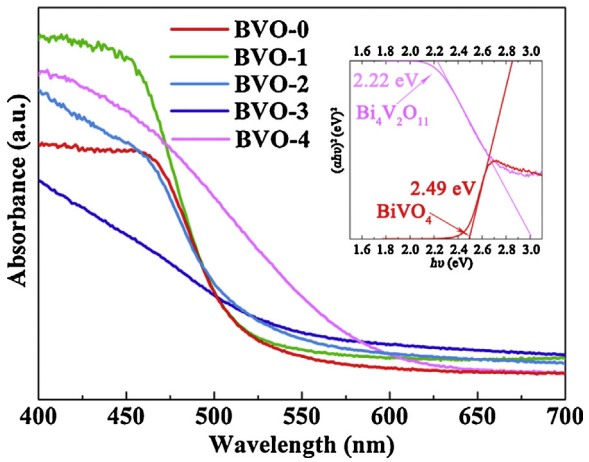

Fig. 10. UV–vis diffuse reflectance spectrum of as-calcinated samples and the insert image is the plots of $(\alpha h\nu)^{n/2}$ vs $h\nu$ ($n = 4$).

most superior activity among the samples (Fig. S3). As BVO-1 possesses favourable nanosized interfacial contact, it is presumed that the superior photocatalytic properties for BVO-1 could be ascribed to nanosized interfacial contact.

In order to attest above conjecture, photocurrent transient response measurements of the samples are performed (Fig. 9). As shown in Fig. 9, all the electrodes are prompt in generating photocurrent with a reproducible response to on/off cycle, demonstrating that photoinduced carriers could transfer effectively and electrons collect successfully for the samples. Compared with BVO-0 and BVO-4, the heterojunction samples exhibit enhanced photocurrent intensity. It could be inferred that the construction of $BiVO_4/Bi_4V_2O_{11}$ element-copied heterojunction could effectively promote the transfer and separation of photoinduced carriers. Nevertheless, it is worthy of noticing that the BVO-1 film electrode shows rather remarkable enhanced current intensity than other heterojunction samples and a 10-fold enhancement than BVO-0. This enhancement could be attributed to the favourable nanosized interfacial contact in BVO-1. And the excellent transfer efficiency of the photoinduced charge carriers determines the outstanding photocatalytic properties of BVO-1.

The optical properties of as-calcinated samples are measured by UV–vis diffuse reflectance spectrum (Fig. 10). All of them show strong absorption in visible light region and the absorption edge exhibit a gradual red shift as the mole quantities of Bi increase, and the BVO-4 possesses the most powerful light absorption ability. The insert image shows the bandgap of BVO-0 and BVO-4 estimated from the main absorption edge of the UV–vis diffuse reflectance spectrum.

The VBM for BVO-0 and BVO-4 is measured by valence band XPS (Fig. 11a). The edge of the maximum energy of BVO-0 nanofibres is located at about 1.48 eV, while the BVO-4 displays 1.65 eV for the edge of the maximum energy. Even though $Bi_4V_2O_{11}$ is element-copied as $BiVO_4$, the distinction in crystalline structure and stoichiometry ratio can result in different band structure for $Bi_4V_2O_{11}$, which is similar to previous work [14,15,38,39]. Hence, the inconsistency exists in VB of $Bi_4V_2O_{11}$. Combined with the results of optical measurements and valence band position analysis, a schematic illustration of potential energy for $BiVO_4$ and $Bi_4V_2O_{11}$ is shown in Fig. 11b. In addition, these two semiconductors show a well staggered band alignment.

Based on the above experimental results and theory analysis, a proposed mechanism of photocatalytic reactions happened on BVO-1 is illustrated in Fig. 12. Moreover, both the staggered energy band and nanosized interfacial contact are favorable for the separation and transfer of electron-hole pairs with an internal built-up electric field at the interfaces. The small size of $Bi_4V_2O_{11}$ nanocrystals could also cause a decreased carriers transport pathway, which could facilitate the separation and transfer of photoinduced charge carriers. As a consequence, the recombination of the photoinduced electron-hole pairs is greatly reduced and the charge carriers lifetime is prolonged for BVO-1. However, further increasing the amount of Bi could result in an counterproductive effect. The density of nanosized interfacial contact is declined because of harvesting more $Bi_4V_2O_{11}$ particles with large size. Thus, the BVO-2 and BVO-3 heterojunction nanofibres do not behave better on photocatalytic performance compare with BVO-1.

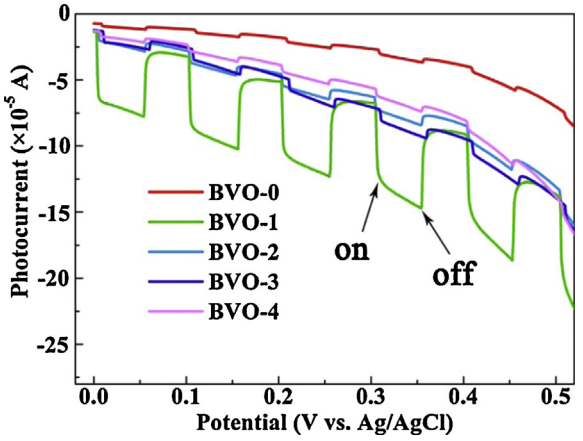

Fig. 9. Photocurrent plot of as-calcinated samples photoeletrodes.

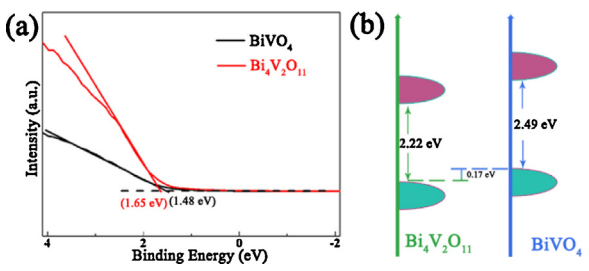

Fig. 11. (a) Valence band spectra of BVO-0 and BVO-4; (b) schematic illustration of $BiVO_4/Bi_4V_2O_{11}$ band alignment.

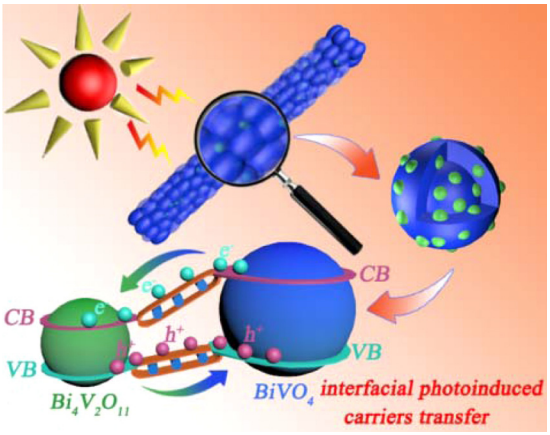

Fig. 12. The photocatalytic mechanism illustration of hybrid nanofibres.

4. Conclusions

We have demonstrated the fabrication of $BiVO_4/Bi_4V_2O_{11}$ element-copied heterojunction nanofibres to realize nanosized interfacial contact. It was proposed that the element-copied semiconductors selection were critical for the formation of nanosized interfacial contact. The heterojunction nanofibres with more nanosized interfacial contact was the best-performing one in photocatalysis. As we have indicated the insights into the formation mechanism of nanosized interfacial contact and the interfacial chemical bonding structures of these heterojunction nanofibres, we hope this work might bring revelation to the rational construction of more nanosized heterojunction with accompanying applications in photocatalytic water purification and other fields.

Acknowledgements

This work was financially supported by projects of Natural Science Foundation of China (21271055, 21471040), the Fundamental Research Funds for the Central Universities (HIT. IBRSEM. A. 201410) and Open Project of State Key Laboratory of Urban Water Resource and Environment, Harbin Institute of Technology (QAK201304) and Program for Innovation Research of Science in Harbin Institute of Technology (B201412, B201508) .

Appendix A. Supplementary data

Supplementary data associated with this article can be found, in the online version, at http://dx.doi.org/10.1016/j.apcatb.2015.05.022

References

[1] C. Chen, W.M. Cai, M.C. Long, B.X. Zhou, Y.H. Wu, D.Y. Wu, Y.J. Feng, ACS Nano 4 (2010) 6425–6532.
[2] X.H. Gao, H.B. Wu, L.X. Zheng, Y.J. Zhong, Y. Hu, X.W. Lou, Angew. Chem. Int. Ed. 125 (2014) 6027–6031.
[3] H.L. Wang, L.S. Zhang, Z.G. Chen, J.Q. Hu, S.J. Li, Z.H. Wang, J.S. Liu, X.C. Wang, Chem. Soc. Rev. 43 (2014) 5234–5244.
[4] H. Xu, S.X. Ouyang, L.Q. Liu, P. Reunchan, N. Umezawa, J.H. Ye, J. Mater. Chem. A 2 (2014) 12642–12661.
[5] X. Li, J.G. Yu, J.X. Low, Y.P. Fang, J. Xiao, X.B. Chen, J. Mater. Chem. A 3 (2015) 2485–2534.
[6] Z.C. Zhang, B. Xu, X. Wang, Chem. Soc. Rev. 43 (2014) 7870–7886.
[7] J. Junquera, M. Zimmer, P. Ordejón, P. Ghosez, Phys. Rev. B 67 (2003) 155327.
[8] M.T. Niu, F. Huang, L.F. Cui, P. Huang, Y.L. Yu, Y.S. Wang, ACS Nano 4 (2010) 681–688.
[9] M. Berr, A. Vaneski, A. Susha, J. Rodríguez-Fernández, M. Döblinger, F. Jäckel, A. Rogach, J. Feldmann, Appl. Phys. Lett. 97 (2010) 093108.
[10] L. Amirav, A. Alivisatos, J. Phys. Chem. Lett. 1 (2010) 1051–1054.
[11] B. Xu, P.P. He, H.L. Liu, P.P. Wang, G. Zhou, X. Wang, Angew. Chem. Int. Ed. 53 (2014) 2339–2343.
[12] L. Zhang, D.W. Jing, X.L. She, H.W. Liu, D.J. Yang, Y. Lu, J. Li, Z.F. Zheng, L.J. Guo, J. Mater. Chem. A 2 (2014) 2071–2078.
[13] J. Li, L.Z. Zhang, Y.J. Li, Y. Yu, Nanoscale 6 (2014) 167–171.
[14] L. Wang, J. Shang, W.C. Hao, S.Q. Jiang, S.H. Huang, T.M. Wang, Z.Q. Sun, Y. Du, S.X. Dou, T.F. Xie, D.J. Wang, J. Wang, Sci. Rep. 4 (2014) 7384.
[15] J. Shang, W.C. Hao, X.J. Lv, T.M. Wang, X.L. Wang, Y. Du, S.X. Dou, T.F. Xie, D.J. Wang, J.O. Wang, ACS Catal. 4 (2014) 954–961.
[16] X. Xiao, R.P. Hu, C. Liu, C.L. Xing, X.X. Zuo, J.M. Nan, L.S. Wang, Chem. Eng. J. 225 (2013) 790–797.
[17] S.M. Sun, W.Z. Wang, L. Zhang, L. Zhou, W.Z. Yin, M. Shang, Environ. Sci. Technol. 43 (2009) 2005–2010.
[18] X.F. Chen, J.B. Liu, H. Wang, Y.L. Ding, Y.X. Sun, H. Yan, J. Mater. Chem. A 1 (2013) 877–883.
[19] N. Al-Areqi, A. Al-Alas, A. Al-Kamali, K. Ghaleb, K. Al-Mureish, J. Mol. Catal. A 381 (2014) 1–8.
[20] Z.F. Huang, J.J. Song, L. Pan, F.L. Lv, Q.F. Wang, J.J. Zou, X.W. Zhang, L. Wang, Chem. Comm. 50 (2014) 10959–10962.
[21] Z.F. Huang, J.J. Song, L. Pan, X. Jia, Z. Li, J.J. Zou, X.W. Zhang, L. Wang, Nanoscale 6 (2014) 8865–8875.
[22] Z.Y. Zhang, C.L. Shao, X.H. Li, Y.Y. Sun, M.Y. Zhang, J.B. Mu, P. Zhang, Z.C. Guo, Y.C. Liu, Nanoscale 5 (2013) 606–618.
[23] P. Kumar, J. Sundaramurthy, S. Sundarrajan, V. Babu, G. Singh, S.I. Allakhverdievef, S. Ramakrishna, Energy Environ. Sci. 7 (2014) 3192–3222.
[24] J. Tian, Z.H. Zhao, A. Kumar, R. Boughton, H. Liu, Chem. Soc. Rev. 43 (2014) 6920–6937.
[25] X. Zhang, C.L. Shao, Z.Y. Zhang, J.H. Li, P. Zhang, M.Y. Zhang, J.B. Mu, Z.C. Guo, P.P. Liang, Y.C. Liu, ACS Appl. Mater. Interfaces 4 (2012) 785–790.
[26] D. Li, Y.N. Xia, Nano Lett. 3 (2003) 555–560.
[27] M. Shang, W.Z. Wang, J. Ren, S.M. Sun, L. Wang, L. Zhang, J. Mater. Chem. 19 (2009) 6213–6218.
[28] S.W. Liu, K. Yin, W.S. Ren, B. Cheng, J.G. Yu, J. Mater. Chem. 22 (2012) 17759–17767.
[29] Z.S. Liu, J.N. Niu, P.Z. Feng, Y.W. Sui, Y.B. Zhu, RSC Adv. 4 (2014) 43399–43405.
[30] N. Tian, Y. Huang, Y.X.T.R. Guo Zhang, Y.H. Zhang. Daltion Trans.
[31] A. Booshehri, S. Goh, J.D. Hong, R.R. Jiang, R. Xu, J. Mater. Chem. A 2 (2014) 6209–6217.
[32] L.A. Anh, T. Rai, J. Thi, S. Gim, E. Kim, Shin, J. Lee, J. Kim, J. Power Sources 243 (2013) 891–898.
[33] X.H. Li, H.Y. Xu, X.T. Zhang, Y.C. Liu, J.W. Sun, Y.M. Lu, Appl. Phys. Lett. 95 (2009) 191903.
[34] S. Patwe, A. Patra, R. Dey, A. Roy, R. Kadam, S. Achary, A. Tyagi, J. Am. Ceram. Soc. 96 (2013) 3448–3456.
[35] S. Kumar, P. Sahare, Nano 8 (2013) 1350007.
[36] B. Tatar a, K. Kutlu, M. Ürgen, Thin Solid Films 516 (2007) 13–16.
[37] G. Schwartz, M. Hybertsen, J. Bevk, R. Nuzzo, J. Mannaerts, G. Gualtieri, Phys. Rev. B 39 (1989) 1235–1241.
[38] J.L. Wang, Y. Yu, L.Z. Zhang, Appl. Catal. B 136-137 (2013) 112–121.
[39] Q.C. Liu, D.K. Ma, Y.Y. Hu, Y.W. Zeng, S.M. Huang, ACS Appl. Mater. Interfaces 5 (2013) 11927–11934.